Catalysis Science & Technology

ROYAL SOCIETY OF CHEMISTRY

PAPER

View Article Online
View Journal | View Issue

Cite this: *Catal. Sci. Technol.*, 2025, **15**, 1041

An examination of dimethyl oxalate hydrogenation to methyl glycolate on silica-supported Ni–Co alloy catalysts†

Donghui Xiao,[a] Shilong Xie,[a] Xin Gao, *[a] Riguang Zhang[b] and Chun-Ran Chang *[ac]

The selective hydrogenation of dimethyl oxalate (DMO) to methyl glycolate (MG) is becoming increasingly attractive for the industrial production of polyglycolic acid (PGA) biodegradable plastics. However, it is still necessary to develop highly selective/active and affordable DMO hydrogenation catalysts for the large-scale production of MG and PGA. In this report, silica-supported Ni–Co alloy catalysts were meticulously investigated for the selective hydrogenation of dimethyl oxalate to methyl glycolate. Compared with monometallic Ni or Co, the supported Ni–Co alloy catalysts with an appropriate doping of Co in Ni resulted in the significant promotion of dimethyl oxalate conversion and methyl glycolate selectivity at mild temperature (180 °C). Optimized dimethyl oxalate conversion and selectivity for methyl glycolate were 87% and 86%, respectively, on the 15Ni–10Co/SiO_2 catalyst. The promotion of dimethyl oxalate conversion was attributed to the large capacity and strong strength of hydrogen adsorption, as proven *via* H_2-TPD, and the active sites with uniform strength for CO adsorption and dimethyl oxalate (or key oxygenated intermediates) adsorption, as proven *via in situ* CO-DRIFTS. These phenomena were enhanced by the effective interaction between Ni and Co. Furthermore, it was found that the strength of acid sites has an influence on product selectivity control for ethanol and methyl formate; particularly, the synergy between the acid sites and metal sites may facilitate deep hydrogenation of dimethyl oxalate to form unexpected methyl formate. This study not only shows the catalytic behavior of dimethyl oxalate hydrogenation on non-precious Ni–Co alloy catalysts but also provides new insights into designing Ni-based catalysts for the selective hydrogenation of oxygenates with multiple ester groups.

Received 23rd October 2024,
Accepted 27th December 2024

DOI: 10.1039/d4cy01278j

rsc.li/catalysis

1. Introduction

Many studies have shown that millions of tons of non-biodegradable waste plastics are increasingly discarded in the natural environment globally each year.[1] Environmental pollution caused by these non-biodegradable waste plastics poses serious hazards to human life and health.[2,3] Polyglycolic acid (PGA), an important downstream product of the polymerization of methyl glycolate (MG), is a polymer material with good biodegradability and biocompatibility. Its mechanical strength, barrier and heat resistance are extremely outstanding, and it can be widely used in a variety of applications, such as food packaging, oil and gas exploration, biomedicine, and agricultural production.[4–7] Thus, to cope with the far-reaching impact on the environment caused by the inability of polyolefin plastics to degrade naturally, the development of degradable PGA materials is of great significance to environmental governance and economic and social development.[8,9]

Since the 1960s, the chemical and pharmaceutical industries have been conducting in-depth research on methods for the preparation of MG monomers. The preparation process for hydrolysis of chloroacetic acid is simple and its reaction conditions are mild, but the process flow is long and the reaction process requires harsh raw materials such as sodium hydroxide and concentrated sulfuric acid. Moreover, it faces disadvantages such as low yield and serious corrosion of equipment.[10] Alternatively, the MG yield of the formaldehyde and hydrocyanic acid addition method is higher, but the reaction of the raw material hydrocyanic acid is toxic and not in line with the requirements of green chemistry in industry.[11] The one-step synthesis method of direct oxidation of glyoxal or

[a] *Shaanxi Key Laboratory of Energy Chemical Process Intensification, School of Chemical Engineering and Technology, Xi'an Jiaotong University, Xi'an 710049, China. E-mail: xggao@xjtu.edu.cn, changcr@mail.xjtu.edu.cn*
[b] *State Key Laboratory of Clean and Efficient Coal Utilization, College of Chemical Engineering and Technology, Taiyuan University of Technology, Taiyuan, Shanxi 030024, China*
[c] *Shaanxi Key Laboratory of Low Metamorphic Coal Clean Utilization, School of Chemistry and Chemical Engineering, Yulin University, Yulin 71900, China*
† Electronic supplementary information (ESI) available: [DETAILS]. See DOI: 10.1039/d4cy01278j

ethylene glycol and methanol has high raw material utilization rate and short process flow, but faces shortcomings, for instance, high cost of raw materials and catalysts, and difficult separation of products, limiting the large-scale production of MG.[12,13] Energy chemicals using syngas as a raw material have achieved vigorous development in recent years. Among them, the conversion of syngas to generate dimethyl oxalate (DMO) has been industrialized. Thus, DMO hydrogenation presents a promising opportunity for the synthesis of MG, which has been gained extensive attention in academia and industry.[14,15]

The central goal for improving the reaction performance of selective DMO hydrogenation to MG is the development of efficient catalysts. At the present stage, the catalytic systems applied in the hydrogenation of DMO to MG are mainly divided into homogeneous catalysts, represented by noble metal Ru complexes, and heterogeneous catalysts, represented by loaded Cu and Ag. Among the former, the homogeneous Ru complex catalysts are complicated to prepare and difficult to recycle, making their application difficult in large-scale industrial production, and the use of noble metals increases the cost of catalysts.[16,17] Among the heterogeneous catalysts, Cu-based catalysts are easy to completely hydrogenate DMO to form ethylene glycol (EG) and ethanol (ET) due to their strong ability to activate molecular hydrogen and the reaction intermediates, resulting in low MG selectivity.[18–20] For example, Wang *et al.* synthesized a series of catalysts by ammonia evaporation, and the MG selectivity of Cu/SiO_2 catalysts was 40% and that of Cu/ZrO_2 catalysts was 47% at 200 °C.[18] Abbas *et al.* used hydrothermal and acoustic methods to prepare catalysts, and the MG selectivity of the noble metal-free Cu/SiO_2 catalyst synthesized by the acoustic chemical method was 94%, while the MG selectivity of the catalyst synthesized by the hydrothermal method was 81%.[19] Zhang *et al.* prepared copper catalysts embedded with N-doped carbon microspheres (Cu@NC) *via* a one-pot hydrothermal method, and the MG selectivity was 80.3% in a long-term evaluation of 220 h.[20] In contrast, although Ag-based catalysts can achieve higher MG yields, the cost of noble metal catalysts prevents the development of large-scale production and the reaction usually needs to be carried out at temperatures higher than 200 °C, which increases the operation cost and energy consumption.[21–23] For instance, Wang *et al.* prepared Ag–Ce/ZrO_2 catalysts with different contents *via* the equal volume impregnation method, and the conversion of DMO was 94.28% and the selectivity for MG was 85.80% at 210 °C with the addition of 1 wt% of Ce.[21] Dong *et al.* developed MSNS carriers *via* the biphasic stratification approach and used a post-grafting strategy for the silylation of APTS. The MG selectivity of the Ag/MSNS catalyst was 96.6% and the DMO conversion was 94.28% at 220 °C, while the MG selectivity of the Ag/NH_2-MSNS catalyst remained unchanged but the DMO conversion reached 100%.[22] Luo *et al.* investigated the effect of a support on Ag/SiO_2 catalysts prepared *via* the impregnation method at a reaction temperature of 220 °C, and their hydrotreating activity followed the order of Ag/MSNS > Ag/SBA-15 > Ag/G6, while the MG selectivity followed the order of Ag/G6 > Ag/MSNS > Ag/SBA-15.[23] Therefore, the exploitation of non-precious metal catalysts for efficient and highly selective/active DMO hydrogenation under mild conditions is significant.

However, although Ni-based and Co-based catalysts have demonstrated outstanding capability in the hydrogenation of unsaturated substrates in the literature, their catalytic performances have been rarely studied in the hydrogenation of DMO, where only Ni or Co phosphide catalysts were reported to achieve the optimized catalytic efficiencies.[24,25] For instance, Zhu *et al.* prepared Ni foam-supported Ni_3P catalysts for the hydrogenation of dimethyl oxalate and achieved high selectivity for methyl glycolate of 95% at 230 °C.[24] Zhuang *et al.* studied the effect of the ratio between Co and P, and applied the Co_8P/SiO_2 catalyst, achieving the selectivity for methyl glycolate of 88.1% and dimethyl oxalate conversion of 94.6% at 240 °C.[25] However, the reaction performances and mechanisms on both monometallic Ni and Co catalysts still remain unclear in DMO hydrogenation. In addition, the preparation of metal phosphide catalysts is known to be toxic to the environment and the reported reaction temperatures are relatively high. Therefore, considering the synergistic effects in dual metal or alloy systems rather than single metals,[26,27] it is very meaningful to deeply understand the DMO hydrogenation not only on monometallic Ni and Co catalysts but also on Ni–Co bimetallic systems. In this respect, Ni and Co possess similar atomic sizes and comparable chemical properties, contributing to the formation of a stable bimetallic or alloy structure.[28]

Herein, we conducted a comprehensive study on supported Ni and Co catalysts and designed Ni–Co alloy-supported SiO_2 for the selective hydrogenation of DMO to MG at mild temperature (180 °C) with up to 87% DMO conversion and 86% MG selectivity (Fig. 1). It was found that the product selectivity on different Ni-based bimetallic catalysts varied considerably after the addition of Co element due to the effects from the bimetallic interaction between Ni and Co, and all the catalysts achieved a certain amount of improvement in DMO conversion compared with the Ni-based catalysts. Leveraging various characterization tools, the optimal Ni and Co loadings of 15

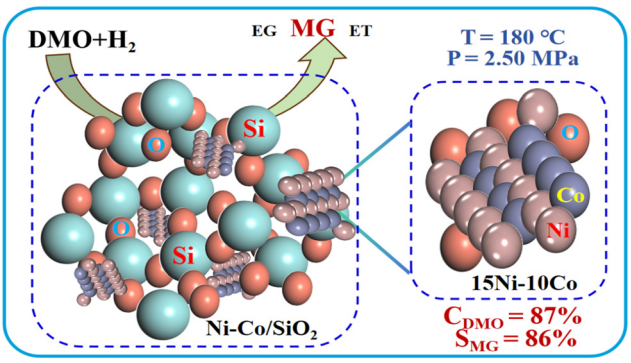

Fig. 1 Schematic description of DMO hydrogenation to produce MG on silica-supported Ni–Co alloy catalysts.

wt% and 10 wt%, respectively, are mainly attributed to several reasons, such as the smaller size of metallic nanoparticles, the excellent capability of hydrogen adsorption, unified active sites with appropriate strength of DMO (or key oxygenated intermediates) adsorption, and the low surface acidity in the alloy structure. This work does not only develop non-precious Ni–Co alloy catalysts for selective DMO hydrogenation, but also provides new insights into the design of Ni-based catalysts for the selective hydrogenation of oxygenates with multiple ester groups.

2. Experimental

2.1 Materials

Nickel nitrate hexahydrate ($Ni(NO_3)_2{\cdot}6H_2O$, 99.9 wt% purity), cobalt nitrate hexahydrate ($Co(NO_3)_2{\cdot}6H_2O$, 99 wt% purity), silica gel (SiO_2, 40–75 μm, 70 Å, BET: 480 $m^2\ g^{-1}$) were purchased from Sigma-Aldrich (St. Louis, MO, USA). Dimethyl oxalate (DMO, 99 wt% purity) was purchased from Meryer (Shanghai) Chemical Technology Co., Ltd. Methanol (CH_3OH, 99.5 wt% purity) and silica wool were purchased from Shanghai Macklin Biochemical Technology Co., Ltd. These reagents and chemicals were used without further purification.

2.2 Preparation of catalysts

The supported catalysts were prepared through the conventional incipient wetness impregnation. Firstly, the commercial SiO_2 was added to deionized (DI) water and washed by ultrasonication at room temperature for 15 min. Then, SiO_2 was filtered using DI water and ethanol three times, followed by drying in an oven at 80 °C for 12 h. Subsequently, SiO_2 was calcinated in a muffle furnace at the heating rate of 3 °C min^{-1} for 6 h at 550 °C. The incipient wetness volume of SiO_2 was calculated to be 1.3 mL g^{-1}. Next, a certain amount of nickel nitrate hexahydrate and a certain amount of cobalt nitrate hexahydrate were simultaneously dissolved in DI water. The solution was ultrasonicated for 30 min, and then added dropwise to the SiO_2 carrier to obtain the Ni_xCo_y catalyst precursor. The catalyst precursor was allowed to stand for 12 h, and then placed in oven at 80 °C for 12 h. The catalyst samples were calcined at 350 °C for 2 h under flowing air (80 mL min^{-1}) at the heating rate of 3 °C min^{-1}. After cooling to room temperature, the samples were reduced under flowing hydrogen at 400 °C for 4 h at the heating rate of 3 °C min^{-1}. Eventually, the catalyst samples were passivated under a flowing 1% v/v O_2/N_2 gas mixture for 15 min at room temperature. The catalyst samples were denoted as xNiyCo/SiO_2, where x and y stand for the weight loading percent (wt%) of Ni and Co, respectively, on SiO_2.

2.3 Catalyst characterization

X-ray diffraction (XRD) patterns were recorded on a Bruker D8 Advance X-ray diffractometer using nickel-filtered Cu Kα radiation (λ = 0.15418 nm), at the voltage and current of 30 kV and 10 mA, respectively, and scanning speed of 6° min^{-1} in the scanning angle (2θ) range of 15–85°.

Nitrogen adsorption and desorption isotherms were recorded using a Micrometrics ASAP 2460 apparatus instrument. The surface area was determined using the Brunauer–Emmett–Teller (BET) method, and the aperture distribution was calculated using the Barrett–Joyner–Halenda (BJH) method.

The actual loadings of all the catalysts were determined *via* ion-coupled plasma optical emission spectroscopy (ICP-OES) on a Thermo Scientific ICAP 7400 spectrometer.

The morphologies of the catalysts were observed through scanning electron microscopy (SEM), transmission electron microscopy (TEM) and energy-dispersive X-ray spectroscopy (EDX) mapping on a GeminiSEM 500 and FEI Talos F200x electron microscope operating at 200 keV.

Hydrogen-temperature programmed reduction (H_2-TPR) measurements were performed on an Autosorb-iQC-TPX from Quantachrome. In this experiment, 100 mg of sample was pre-treated at 150 °C (heating rate of 10 °C min^{-1}) for 1 h in a flow of He. Subsequently, the sample was cooled down to 50 °C under the same flow of He. The H_2-TPR analysis was performed from 50 °C to 700 °C (10 °C min^{-1}) in a flow of 10 vol% H_2 in He.

The temperature-programmed desorption of hydrogen (H_2-TPD) measurements were performed on an Autosorb-iQC-TPX from Quantachrome. In experiment, 100 mg of sample was pre-treated at 400 °C (heating rate of 10 °C min^{-1}) for 2 h in a flow of 10 vol% H_2 in He. Subsequently, the sample was cooled to 50 °C under the same flow of 10 vol% H_2 in He. Then, the system was purged for 2 h in a flow of He to remove physically adsorbed H_2 molecules. Finally, The H_2-TPD analysis was performed from 50 °C to 700 °C (10 °C min^{-1}) in a flow of He.

Temperature-programmed desorption of ammonia (NH_3-TPD) measurements were performed on an Autosorb-iQC-TPX from Quantachrome. Firstly, 100 mg of sample was pretreated at 400 °C (heating rate of 10 °C min^{-1}) for 2 h in a flow of 10 vol% H_2 in He. Secondly, the system was purged at 250 °C (heating rate of 10 °C min^{-1}) for 2 h in a flow of He to remove both physically and chemically adsorbed H_2 molecules. After cooling to 50 °C, the sample was exposed to an He stream containing 5 vol% NH_3 for 2 h to fully saturate the catalyst surface. Finally, after flushing the system in an He stream for 2 h, NH_3-TPD analysis was performed from 50 °C to 600 °C (10 °C min^{-1}) in an He stream.

X-ray photoelectron spectroscopy (XPS) measurements were performed using a Thermo Fisher Scientific ESCALAB Xi+ instrument equipped with a monochromatic Al Kα X-ray source. For XPS measurements, the catalyst was mounted on conductive tape and adhered to the XPS sample holder. No further processing was performed prior to XPS measurement.

The CO-DRIFTS spectra were recorded using a Bruker INVENIO S FTIR spectrophotometer equipped with a DTGS detector. The catalyst was mixed with KBr in a weight ratio of

1 : 5. Firstly, the sample was pre-treated at 400 °C (heating rate of 10 °C min^{-1}) for 2 h in a stream of H_2. Secondly, the sample was cooled to 50 °C in the same H_2 flow and the system was purged for 2 h in an N_2 flow. Thirdly, the sample was exposed to a flow of N_2 containing 1 vol% CO for 1 h to fully saturate the catalyst. Finally, after purging the system for 1 h in a flow of N_2, background spectra were recorded and CO-DRIFTS spectra were recorded during purging at 160 °C to 220 °C for 60 min.

2.4 Evaluation of DMO hydrogenation reactions

The selective hydrogenation of DMO to MG was performed in a down-flow fixed-bed reactor (300 mm length by 8 mm inner diameter stainless steel) using methanol-DMO (15 wt%). A certain amount of catalyst mixed with quartz sand was placed in the central constant temperature zone of the reactor, and the upper and lower sections of the catalyst were filled with quartz cotton, respectively. The catalyst was activated for 4 h at 400 °C in an H_2 atmosphere. After, the reactor temperature was cooled to the reaction temperature (170–220 °C) and the reaction pressure (1.0–3.0 MPa) was adjusted to the set value. Then, DMO dissolved in methanol was introduced in the reactor from the top of the reactor with hydrogen gas at a specific flow rate set by the high-pressure liquid feed pump to participate in the reaction. Finally, the products were collected in a condenser (3 °C) and analyzed using a PANNA 1949 gas chromatography-flame ionization detector (GC-FID) with a 30 m HP-INNOWax capillary column (DIMKA). The DMO conversion and product selectivity were defined as follows:

$$\text{DMO conversion (\%)} = \frac{\sum f_i A_{i,\text{out}}}{f_{\text{DMO}} A(\text{DMO})_{\text{in}}} \times 100\%$$

$$\text{Selectivity (\%)} = \frac{f_i A_{i,\text{out}}}{\sum f_i A_{i,\text{out}}} \times 100\%$$

where $A_{i,\text{out}}$ and f_i are the chromatographic peak area at the outlet and the relative molar calibration factor of the individual product i (i = MG, ethylene glycol, ethyl alcohol, methyl acetate, 1,2-propanediol, 1,2-butanediol, 2-methoxyethanol, and 2-ethoxyethanol), respectively.

3. Results and discussion

3.1 Textural properties of supported Ni–Co alloy catalysts

The actual contents of Ni and Co were measured by ICP-OES, as shown in Table 1, and the theoretically calculated values of the catalysts were close to the actual ICP test values, indicating that the chosen isovolumetric impregnation method has a high atom utilization rate.[29,30]

The pore structures of the prepared catalysts were tested by nitrogen physical adsorption and desorption, as shown in Fig. S1–S6,† where the adsorption isotherms of all the supported Ni–Co bimetallic catalysts had hysteresis loops between the relative pressures of 0.4 and 0.98, and there was a partial volume increment with an increase in the relative pressure, which conformed to the class IV adsorption isotherm according to the classification of IUPAC, and constituted the obvious H4-type hysteresis loops with the desorption curves, indicating that the catalysts are rich with mesopores.[31]

The textural properties of the supported Ni–Co bimetallic catalysts were analyzed. As shown in Table 1, both the specific surface area and pore volume of all the supported catalysts are lower than that of the silica support, suggesting the deposition of Ni and Co on the internal surface of the silica support. In addition, no significant change in the average pore diameters of all the supported catalysts compared to the silica support was observed, which can once more identify that the Ni and Co nanoparticles were deposited on the internal surface and no pore blockage occurred.[32] By employing XRD, the average diameters of the metallic nanoparticles on all the supported catalysts were analyzed. The largest average nanoparticle diameter was measured to be 23.72 nm on 15Ni/SiO_2; conversely, despite the use of the same catalyst preparation method, 15Co/SiO_2 possessed the lowest average nanoparticle diameter of 6.27 nm. This indicates that the intrinsic interaction between Ni and SiO_2 is weaker than that between Co and SiO_2. Next, the Ni–Co bimetallic nanoparticles dramatically shrunk from 12.79 nm when 3 wt% of Co was doped into 15 wt% of Ni. Thus, this evidently proves that the synergetic effect between Ni and Co allows the better dispersion of Ni atoms. The Ni–Co bimetallic nanoparticles maintained a constant size of around 12 nm when the loading of Co increased from 3 wt% to 15 wt%. At this point, it clearly demonstrates that the

Table 1 Textural properties of Ni–Co bimetallic catalysts

Sample name	Preset Ni loading (wt%)	Preset Co loading (wt%)	Actual Ni loading[a] (wt.%)	Actual Co loading[a] (wt.%)	S_{BET} (m^2 g^{-1})	V (cm^3 g^{-1})	D_p (nm)	Particle size[b] (nm)
SiO_2	—	—	—	—	483.43	0.75	6.03	—
15Ni/SiO_2	15	0	14.93	0	258.41	0.41	6.12	23.72
15Ni–3Co/SiO_2	15	3	14.67	2.95	386.94	0.55	5.69	12.79
15Ni–10Co/SiO_2	15	10	14.93	10.08	362.84	0.5	5.55	11.86
15Ni–15Co/SiO_2	15	15	14.92	15.32	304.18	0.45	5.91	12.56
15Co/SiO_2	0	15	0	14.97	315.18	0.51	6.23	6.27

[a] Measured *via* ICP-OES. [b] Calculated using XRD results and the Scherrer equation.

strong interaction between Ni and Co can ensure that the Ni–Co bimetallic nanoparticles with a size of ~12 nm could remain stable enough although the total weight loading of bimetals increased from 18 wt% (15 wt% Ni + 3 wt% Co) to 30 wt% (15 wt% Ni + 15 wt.% Co).

3.2 Phase structure of supported Ni–Co alloy catalysts

The bulk phase compositions of the supported Ni–Co catalysts were carefully analyzed by XRD, as shown in Fig. 2(A). Initially, the XRD peak appeared at 21.98° for the pure SiO_2 carrier. This can be attributed to the characteristic peak for the (101) facet of SiO_2 according to the XRD standard spectrum (PDF#76-0940). Thus, it is reasonable to find the existence of the SiO_2 characteristic peak for all the prepared catalysts. In the case of the monometallic Ni catalyst (15Ni/SiO_2), multiple characteristic peaks of X-ray diffraction are displayed in the spectrum. In detail, the major X-ray diffraction peaks are located at the 2θ values of 44.5°, 51.8° and 76.3°, which are attributed to the characteristic peaks of the Ni (111), Ni (200) and Ni (220) crystal planes, respectively, as referred by the XRD standard spectrum (PDF#70-1849). In addition, the very minor peak for NiO (111) at 37.2° originated from either the interface between Ni and SiO_2 in the form of Ni–O–Si or the passivation of surface and sub-surface of the Ni catalyst after its preparation. In the case of the monometallic Co catalyst (15Co/SiO_2), two characteristic peaks were detected at 36.6° and 43.6° in the XRD spectrum, which correspond to the crystal facets of CoO (111) and Co (101), respectively. Besides, two other small peaks appeared at 61.7° and 74.3°, which are assigned to the CoO (220) and CoO (311) crystal facet, respectively according to the XRD standard spectrum (PDF#70-2856). Analogously, the amount of CoO bulk phase in the 15Ni/SiO_2 catalyst may be dominantly attributed to the incomplete reduction of CoO, which was further confirmed by H_2-TPR. Next, for the supported Ni–Co catalysts with various Co doping loadings, it was transparent to see that all the characteristic peaks of the supported Ni–Co catalysts are located between the monometallic Ni and Co catalysts, and no additional new peaks that represent a heterogeneous phase were generated. This evidently identified the well-formed bimetallic alloy structure.[33,34]

Moreover, based on the X-ray diffraction profiles of the monometallic Ni catalyst, monometallic Co catalyst, and the supported Ni–Co catalysts, the average grain size of the metallic nanoparticles were calculated using the Scherrer equation (Table 1). According to the comparison of the average grain sizes, it was directly found that the monometallic Ni catalyst possessed the largest nanoparticles size of 23.72 nm. Alternatively, the monometallic Co catalyst had a much smaller size of 6.27 nm, which manifests that the intrinsic interaction between Ni and SiO_2 is stronger than the interaction between Co and SiO_2. When Co was doped into the Ni nanoparticles with the loading of 3 wt%, 10 wt% and 15 wt%, the size of the Ni nanoparticles shrunk in half to about 12.79 nm, 11.86 nm and 12.56 nm, respectively. This soundly reveals the interaction between Ni and Co and that

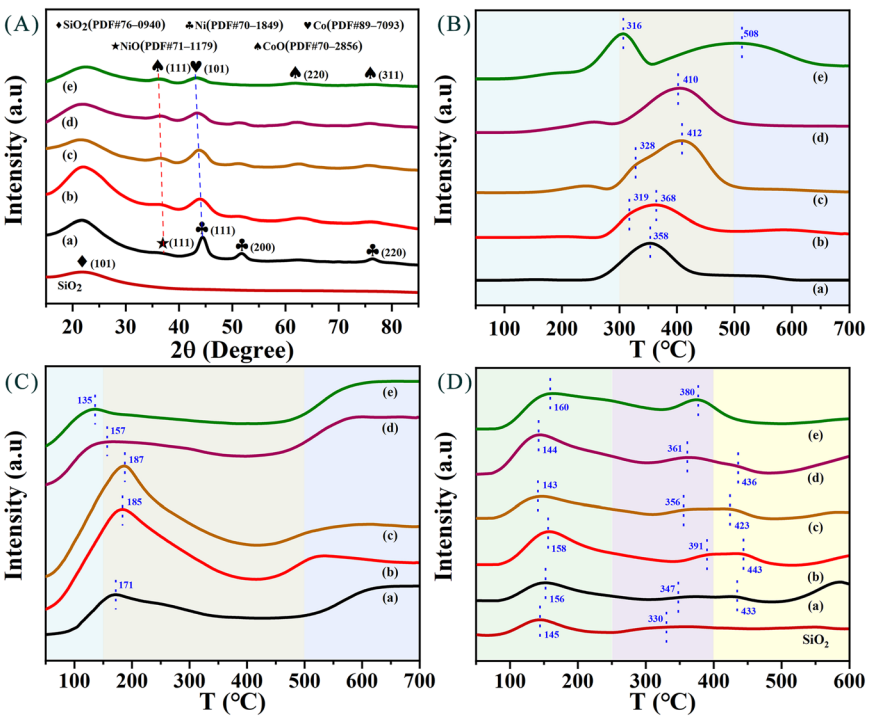

Fig. 2 (A) XRD spectra, (B) H_2-TPR patterns, (C) H_2-TPD patterns, and (D) NH_3-TPD patterns of the supported Ni–Co catalysts. (a) 15Ni/SiO_2, (b) 15Ni–3Co/SiO_2, (c) 15Ni–10Co/SiO_2, (d) 15Ni–15Co/SiO_2, and (e) 15Co/SiO_2.

the doping of Co element dramatically affected the size of the Ni nanoparticles, further benefitting the dispersion of Ni and exposure of the active sites for DMO hydrogenation.[35]

3.3 Morphological structure of supported Ni–Co alloy catalysts

The morphology and elemental distribution of the supported Ni–Co alloy catalysts were analyzed by SEM, TEM and EDX, and the results are shown in Fig. 3. According to the SEM morphology of silica, it can be seen that the silica carrier is a regular sphere with clear edges and no obvious agglomeration, possessing a diameter of about 200 nm. This size provides a suitable specific surface area in the catalytic reaction, which contributes to the improvement of the overall performance of the catalyst. In addition, this regular spherical structure also helps to achieve better heat and mass transfer efficiency in the catalytic bed. The transmission electron microscopy analysis of the 15Ni–10Co/SiO_2 catalyst showed that the Ni–Co nanoparticles were tightly attached to the silica carriers, and the average particle size of the active phases in the 15Ni–10Co/SiO_2 catalyst was in the range of 10–12 nm, which is in agreement with the results of the XRD calculations. Combined with the EDX results, it was found that the Ni and Co nanoparticles were uniformly dispersed on the SiO_2 carriers without obvious aggregation or segregation. This uniform elemental distribution helps more active sites participate in the catalytic reaction, thus maximizing the activity of the catalyst.

3.4 Reducibility of supported Ni–Co alloy catalysts

To explore the bulk properties of the bimetallic materials and the essential metal–metal (here Ni–Co) interaction, the hydrogen reduction properties of the various supported nickel–cobalt alloy catalysts were analyzed by temperature programmed reduction of hydrogen, and the results are displayed in Fig. 2(B). Firstly, it is straightforward to see that the hydrogen reduction peak temperatures on the Ni and Ni–Co catalysts are mainly in the range of 300 °C to 500 °C; however, the monometallic Co catalyst reduction peak temperature is much broader with two major peaks from around 250 °C to 600 °C. In detail, the reduction peak of the 15Ni/SiO_2 catalyst at 358 °C is attributed to the reduction of NiO to Ni, the reduction peak of the 15Co/SiO_2 catalyst at 316 °C corresponds to the reduction of Co_3O_4 to CoO, and the reduction peak at 508 °C in the high-temperature region is attributed to the reduction of CoO to Co. All these observations may directly indicate the presence of NiO species in 15Ni/SiO_2 and the presence of both Co_3O_4 and CoO species in 15Co/SiO_2, which are consistent with the XRD

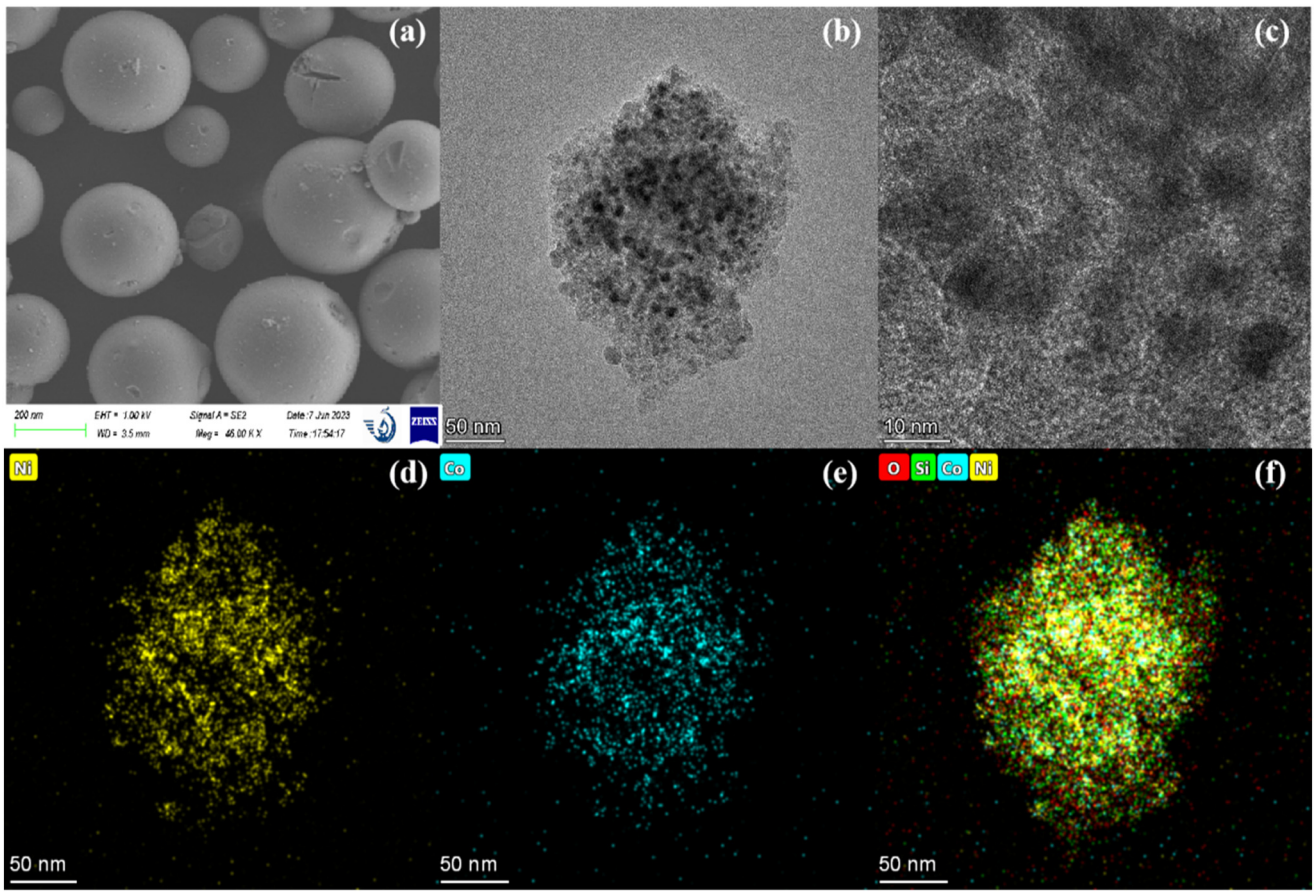

Fig. 3 (a) SEM images of SiO_2 carrier; (b and c) TEM images of the 15Ni–10Co/SiO_2 catalyst; and (d–f) EDX of the 15Ni–10Co/SiO_2 catalyst.

and XPS results as well as other reports.[36,37] Besides, according to Fig. S7,† the interaction between NiO and SiO_2 and the interaction between CoO and SiO_2 can be proven due to the higher temperature of hydrogen reduction observed on the supported Ni or Co catalysts.

In terms of supported Ni–Co catalysts, the reduction peak of NiO shifted to a higher temperature region with an increase in the weight loading of Co up to 10 wt%, which is reasonable evidence that there is strong bimetallic interaction between Ni and Co in the supported Ni–Co catalysts. When the Co weight loading reached 10 wt%, the reduction peaks of the supported Ni–Co catalysts remained constant at around 412 °C. Furthermore, it is noteworthy that the reduction peak temperature of Co_3O_4 was also promoted in a small range from 319 °C on Co/SiO_2 to 328 °C (the shoulder peak connected with the reduction peak of NiO) on the supported Ni–Co catalysts. Meanwhile, the reduction peak temperature of CoO dramatically diminished from high temperature (508 °C) on the $15Co/SiO_2$ catalyst to low temperature (around 412 °C) together with a big reduction peak for NiO in the supported Ni–Co catalysts. In this case, the doping of a large amount of Ni element with Co particles had a significant influence on the reduction of Co_3O_4 and CoO, where the former required a higher temperature and the latter needed a lower temperature. These reduction behaviors again manifest that there is strong Ni–Co interaction on the supported Ni–Co catalysts. These results are also consistent with the calculated particle size distributions (by XRD) with different loadings of Co element, where the addition of Co can substantially benefit the dispersion of Ni and decrease the metallic particle size on the support. Furthermore, the reported DFT calculations show similar trends for a bimetallic system.[38]

3.5 Hydrogen activation of supported Ni–Co alloy catalysts

Molecular hydrogen activation is a key step in DMO hydrogenation. Thus, to understand the intrinsic efficiency of hydrogen activation on the catalyst surfaces, one can perform the temperature programmed desorption of hydrogen. Based on Fig. 2(C), the hydrogen desorption peaks of $15Ni/SiO_2$, $15Co/SiO_2$ and $15Ni–15Co/SiO_2$ possess a similar shape in a wide temperature range. In the case of the monometallic catalysts, the hydrogen desorption peak temperature of the $15Ni/SiO_2$ surface (171 °C) is higher than that on the $15Co/SiO_2$ surface (135 °C), which demonstrates that the binding strength of hydrogen on the Ni surface is stronger than the binding strength of hydrogen on the Co surface. In addition, it is transparent to find that the area of the hydrogen desorption peak on the $15Ni/SiO_2$ surface is larger than that on the $15Co/SiO_2$ surface. This phenomenon directly indicates the differences in hydrogen adsorption capacity between the surfaces of monometallic Ni and Co catalysts, where the former owns higher hydrogen adsorption storage although the metallic particle size on $15Co/SiO_2$ is much smaller than that on $15Ni/SiO_2$.[39] Overall, these metals may bind hydrogen in medium to strong mode.

Based on the $15Ni/SiO_2$ catalyst, the doping of Co element not only significantly expanded the area of the hydrogen desorption peak but also elevated the desorption peak temperature up to around 187 °C from 171 °C. In detail, the hydrogen desorption peak climbed in a very narrow range of 185 °C on $15Ni–3Co/SiO_2$ and 187 °C on $15Ni–10Co/SiO_2$. Meanwhile, the area of the hydrogen desorption peak almost remained constant between these two catalysts. Interestingly, when the loading of Co element was promoted to 15 w.% ($15Ni–15Co/SiO_2$), the hydrogen desorption peak shrunk to 157 °C with a much smaller area compared to other bimetallic catalysts, which indicates that the optimal loading of Co should be less than 15 wt% for hydrogen activation. According to the above-mentioned informative outcomes, it is can be concluded that the appropriate introduction of Co element is quite helpful to promote the adsorption strength and capacity of hydrogen when the loading of Co is no higher than 10 wt%.

3.6 Surface acidity of supported Ni–Co alloy catalysts

Besides the evaluation of hydrogen adsorption, the surface acidity of supported metallic catalysts can play an essential role in catalytic reactions, such as controlling reaction activity and tuning the product selectivity. For instance, the continuous hydrogenation of DMO can produce not only MG and ethylene glycol but also other chemicals, such as ethanol, methyl acetate, and methyl formate. In this case, the acid sites are typically responsible for the formation of ethanol and methyl acetate *via* the hydrogenation–dehydration of EG and EG, respectively. The cracking of the C–C bond in MG to form methyl formate can also proceed on the acid sites. In this respect, temperature programmed desorption of ammonia (NH_3) was performed to evaluate the surface acidity of the as-prepared catalysts. As shown in Fig. 2(D), three types of ammonia desorption peaks were present in all the catalyst samples. These ammonia desorption peaks commonly correspond to various types of surface acidic strengths including weak acid (<250 °C), medium acid (250–400 °C) and strong acid (>400 °C).[40,41] To accurately compare the number of acid sites with different strengths among the various prepared samples, the quantification of the acid sites is shown in Table S1.†

In the case of monometallic catalysts, both the $15Ni/SiO_2$ and $15Co/SiO_2$ catalysts have a notable ammonia desorption peak for the weak acid sites, where the desorption peak temperature of the former catalyst is 156 °C and the latter is 160 °C. At this point, it is worth noting that the ammonia desorption temperature of the SiO_2 support (145 °C) is lower than that on the monometallic catalysts. Hence, the deposition of Ni or Co on SiO_2 can lead to an increase in the acid strength. According to the quantification of the acid sites (Table S1†), it is imperative to note that the number of weak acid sites on the SiO_2 support and $15Ni/SiO_2$ are much lower than that on $15Co/SiO_2$. SiO_2 possesses the least amount of weak acid sites. Considering the intrinsic acidity of the SiO_2 support, the weak

acid sites of the monometallic catalysts are not only from the SiO_2 support itself but also from either the metal oxides by incomplete reduction or the interface phenomenon between the SiO_2 support and Ni or Co.

In the case of the three supported Ni–Co catalysts, the low-temperature peaks of ammonia desorption reveal that all the bimetallic catalysts possess weak acid sites. As the doping of the Co element continued to increase, the temperature of the ammonia desorption peak dropped to 143 °C on 15Ni–10Co/SiO_2 and 144 °C on 15Ni–15Co/SiO_2 from 158 °C on 15Ni–3Co/SiO_2. However, it is clear to see that the range of peak temperature variation is only 15 °C. Quantitatively, the total number of acid sites (including weak, medium and strong strength) follows the decreasing order of 15Ni–15Co/SiO_2 > 15Ni–3Co/SiO_2 > 15Ni–10Co/SiO_2 among the three supported Ni–Co catalysts. Noteworthily, the total number of acid sites on 15Ni–3Co/SiO_2 and 15Ni–15Co/SiO_2 is close. Moreover, the number of weak acid sites also has the same order for the three supported Ni–Co catalysts. However, the number of weak and strong acid sites decreased in the sequence of 15Ni–3Co/SiO_2 > 15Ni–15Co/SiO_2 > 15Ni–10Co/SiO_2 (Table S1†). In detail, a plateau peak of medium-to-strong ammonia desorption is displayed in wide temperature range on 15Ni–3Co/SiO_2 and 15Ni–10Co/SiO_2, and the number of medium and strong acid sites is equivalent on the above-mentioned two samples. Nonetheless, for 15Ni–15Co/SiO_2, it was found that the number of medium acid sites is much larger than strong acid sites. Essentially, the peaks of medium acid sites on 15Ni–3Co/SiO_2, 15Ni–10Co/SiO_2 and 15Ni–15Co/SiO_2 are located at 391 °C, 356 °C and 361 °C, respectively, where the range of peak temperature variation is 35 °C. The peaks of strong acid sites on 15Ni–3Co/SiO_2, 15Ni–10Co/SiO_2 and 15Ni–15Co/SiO_2 are located at 443 °C, 423 °C and 436 °C, respectively, where the range of peak temperature variation is 20 °C. Among these supported Ni–Co catalysts, the results suggest that the strength of both medium and strong acid sites follow the decreasing sequence of 15Ni–3Co/SiO_2 > 15Ni–15Co/SiO_2 > 15Ni–10Co/SiO_2. These findings indicate that the doping amount of Co element is an important factor in tuning both the quantity and strength of surface acidity on supported Ni–Co alloy catalysts, which can be employed to tune the activity and selectivity of DMO hydrogenation.[42]

3.7 Chemical state of supported Ni–Co alloy catalysts

The elemental valence and elemental composition of the catalyst surface were analyzed by XPS to achieve a deep understanding of the surface structures and functionalities of Ni–Co nanoparticles. In this characterization section, two metallic elements (Ni and Co) were probed at the surface atomic level. Regarding surface Ni examination, the results from 15Ni/SiO_2 and the supported Ni–Co catalysts are displayed in Fig. 4(A). In the Ni 2p spectrum, the characteristic peak and satellite peak of Ni $2p_{3/2}$ are located at about 853 eV and 859 eV, respectively, for all the prepared samples. Besides, a plateau characteristic peak appeared at 854.7 eV on 15Ni–15Co/SiO_2. In the Co 2p spectrum, the major characteristic peak and satellite peak of Co $2p_{3/2}$ are located at about 778 eV and 784 eV, respectively, for all the prepared samples (Fig. 4(B)). In the spectra of 15Co/SiO_2, 15Ni–10Co/SiO_2 and 15Ni–15Co/SiO_2, one additional plateau or shoulder characteristic peak is located at about 780 eV. In the spectrum 15Ni–3Co/SiO_2, two more shoulder characteristic peaks are located at 780 eV and 781 eV.

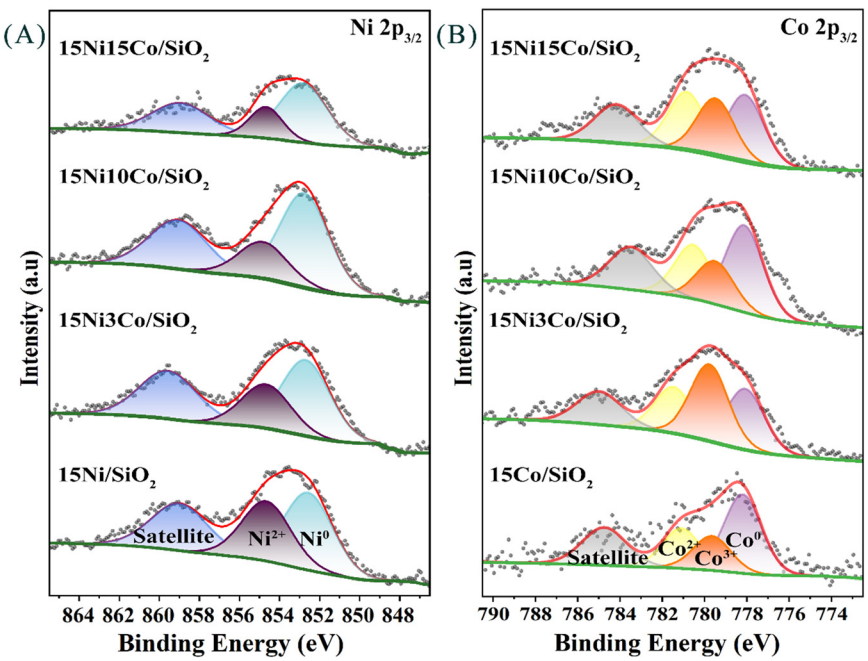

Fig. 4 XPS spectra of various supported Ni–Co catalysts. (A) Ni $2p_{3/2}$ and (B) Co $2p_{3/2}$.

After the peak deconvolution of Ni $2p_{3/2}$ and Co $2p_{3/2}$, zero valence state and oxidized states are displayed in the spectra. In terms of Ni $2p_{3/2}$, Ni^0 and Ni^{2+} are resolved at low and high binding energy, respectively. In the case of Co $2p_{3/2}$, Co^0, Co^{3+} and Co^{2+} are resolved at low, high and middle binding energy, respectively. The existence of oxidized states on Ni and Co can be caused by a few reasons, where one is probably due to the low-concentration oxygen (1% O_2) passivation step during the preparation of the catalyst. A similar measurement on supported Ni-based catalysts was reported by Zhao *et al.*[43] Another reason may be because of the incomplete of metal reduction, which is also reflected by the observed oxide phase in the XRD pattern.

As the doping amount of Co element increased, it was very clear to observe that the binding energies of surface Ni^0 were gradually promoted from 852.6 eV ($15Ni/SiO_2$) to 852.8 eV ($15Ni–15Co/SiO_2$) for Ni^0.[43–45] The binding energy of Ni^{2+} varied in the interval between 854.7 eV and 854.8 eV.[44] In the Co spectra, the binding energy of Co^0 decreased from 778.2 eV to 778.1 eV with an increase in Co doping in the Ni nanoparticles. This tendency demonstrates the effective electronic interaction between Ni and Co by introducing Co element into the Ni nanoparticles.[45] Besides, the binding energy of Co^{3+} and Co^{2+} are located at ~779 eV and ~781 eV, respectively, for all the prepared catalysts.[46,47]

3.8 CO-DRIFTS of supported Ni–Co alloy catalysts

To enhance the understanding of the surface structure and metal–metal interaction on the supported Ni–Co catalysts, a CO-DRIFTS experiment was conducted on the prepared catalyst samples with various loadings of Co doping and at multiple temperatures. The central methodology of this technique is to investigate the surface microenvironment of catalytic materials from the binding modes of the CO molecule. Fig. 5(A) shows the CO-DRIFTS of five different samples including monometallic Ni catalyst, monometallic Co catalyst, and other Ni-based bimetallic catalysts with different quantities of Co. According to the distinguished binding modes of CO, the spectrum is split into three areas with three colors, *i.e.*, orange, pink and green. The three areas, namely 2150 to 2250 cm^{-1}, 2000 to 2150 cm^{-1}, and 1650 to 2000 cm^{-1} represent the CO binding modes of free redial, straight adsorption and bridge adsorption, respectively.[48] Obviously, there is no free-state vibration recorded in the spectra of all the samples, indicating the interference from gaseous CO in the IR band was avoided. The vibrational frequency of CO binding is mainly in the forms of straight and bridge.[49] Among the samples, the monometallic Ni catalyst ($15Ni/SiO_2$) possesses the largest peak areas for the CO adsorption vibrational signals. The adsorption signals from the surface of the monometallic Ni catalyst are located at 2051 cm^{-1}, 1937 cm^{-1} and 1826 cm^{-1}. The first signal can be assigned as the straight adsorption of the CO molecule, while the latter two are related to the doubly bridging binding and triply bridging binding of the CO molecule, respectively. In comparison, although there are similar CO binding modes between the monometallic Ni and Co catalyst, the quantity of CO binding is much lower on the monometallic Co catalyst. Considering the nanoparticle sizes of monometallic Ni and monometallic Co according to XRD, this result can be one important evidence that Ni is much more capable to strongly adsorb molecular CO than Co.

Accompanying the promotion of Co doping into the Ni catalyst from 0 to 10 wt%, the doubly bridging adsorption mode

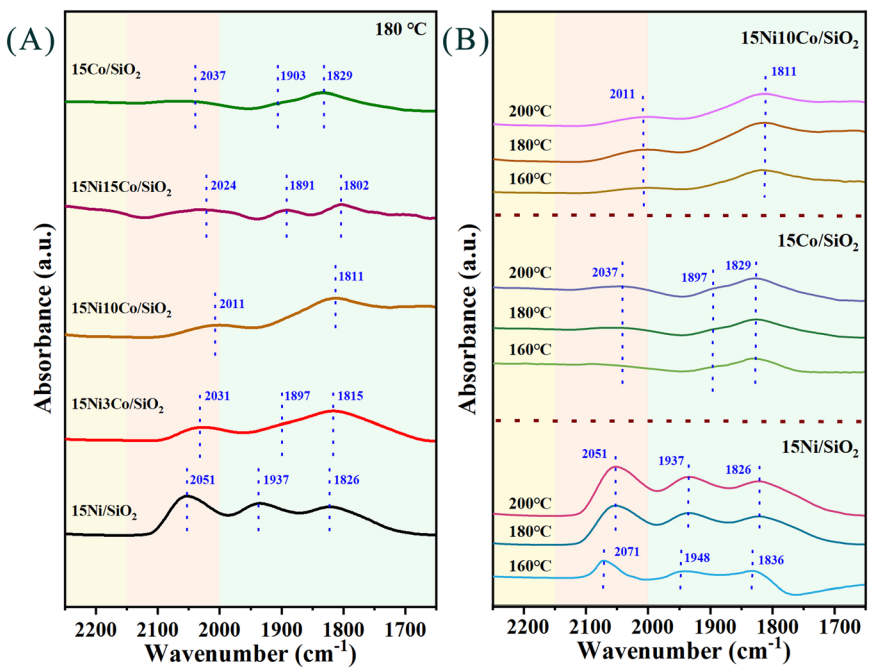

Fig. 5 *In situ* CO-DRIFTS patterns of the as-prepared catalysts. (A) Various supported Ni–Co catalysts and (B) the effect of temperature.

at 1937 cm^{-1} continuously shifted to lower wavenumbers when the Co loading was 3 wt% and 10 wt%, respectively. Besides, the signal peak area of doubly bridging adsorption mode shrunk from 0 to 10 wt% of Co loading, and the corresponding signals are closely connected with the triply bridging adsorption mode at 1826 cm^{-1}. In contrast, when the doping of Co element was set as 15 wt%, the peak area of the doubly bridging adsorption mode increased to a small extent and it could be resolved separately with the signal of triply bridging, as shown in Fig. 5(A). Similar to the CO bridge adsorption described above, the vibrational wavenumber of the CO straight adsorption signal shifted from 2051 cm^{-1} without Co doping to a lower wavenumber at 2022 cm^{-1} (3 wt% Co) and 2011 cm^{-1} (10 wt% Co). Meanwhile, the quantity of CO straight adsorption also decreased when the Co loading increased from 0 to 10 wt%. Nonetheless, the vibrational wavenumber of the CO straight adsorption mode shifted to 2024 cm^{-1} when the Co loading was set as 15 wt%. Moreover, the triply bridging adsorption mode at 1826 cm^{-1} for the monometallic Ni catalyst shifted to a lower vibrational wavenumber with an increase in the quantity of Co doping, such as 1815 cm^{-1} when the Co loading was 3 wt%, 1811 cm^{-1} when the Co loading was 10 wt%, 1802 cm^{-1} when the Co loading was 15 wt%. According to these results, the doping of Co element can lead to the effective interaction of Ni–Co and electron transfer between Ni and Co, further resulting in the formation of stronger CO bridging adsorption modes on the surface of the supported Ni–Co catalysts, and especially intensifying the triply bridging adsorption mode.[50]

According to the comparison of the bimetallic catalysts, although the majority of the CO binding mode is triply bridging adsorption mode on 15Ni–3Co/SiO_2 and 15Ni–10Co/SiO_2, much less CO straight adsorption was observed on 15Ni–10Co/SiO_2, as shown in Fig. 5(A). Considering that the carbonyl groups are usually adsorbed on the metal catalyst surfaces in DMO hydrogenation, herein CO can be regarded as a probe molecule to understand the nature of the active sites that bind oxygen-involved molecules, such as DMO. Thus, according to the above-mentioned description, it is imperative to not only point out that CO binds on the surface of 15Ni–10Co/SiO_2 stronger than the other prepared catalysts but also reveal that the active sites on 15Ni–10Co/SiO_2 are more uniformed for the appropriate strength of CO adsorption and DMO (or key oxygenated intermediates) adsorption.

Next, the CO-DRIFTS on monometallic catalysts and bimetallic catalysts at multiple temperatures at 160 °C, 180 °C and 200 °C are displayed in Fig. 5(B). All the CO binding modes on the 15Ni–10Co/SiO_2 catalyst possess lower vibrational wavenumbers than that on 15Ni/SiO_2 and 15Co/SiO_2. For instance, the wavenumber of CO triply bridging adsorption on 15Ni–10Co/SiO_2 is 1811 cm^{-1}, but the wavenumber of CO triply bridging adsorption on 15Ni/SiO_2 and 15Co/SiO_2 is 1826 cm^{-1} and 1829 cm^{-1}, respectively. This result proves that CO adsorption is always more stable on 15Ni–10Co/SiO_2 rather than on the other monometallic catalysts. One need to notice is that the vibrational wavenumbers of various CO adsorption always remained constant from 160 °C to 200 °C on 15Ni–10Co/SiO_2 and 15Co/SiO_2 except 15Ni/SiO_2. Specially, distinguished shifts appeared for the CO adsorption wavenumber from 160 °C to 180 °C on 15Ni/SiO_2. In this respect, the CO vibrational wavenumber shifted from 2071 cm^{-1} to 2051 cm^{-1} for straight adsorption, from 1948 cm^{-1} to 1937 cm^{-1} for doubly bridging adsorption and from 1836 cm^{-1} to 1826 cm^{-1} for triply bridging adsorption. The reason for the observed shift in the CO oscillation wavenumber may be due to the temperature-dependent interaction between nickel and silica, where the higher the temperature, the stronger the nickel and silica electron transfer and the more stable the CO adsorption pattern. On the contrary, based on the invariant wavenumbers and corresponding peak areas of the various CO adsorption modes on 15Ni–10Co/SiO_2 and 15Co/SiO_2 at all temperatures, it is obvious that the CO adsorption modes on these two catalysts are independent of temperature.

3.9 Reaction testing of supported Ni–Co alloy catalysts

3.9.1 Effects of Co doping. To investigate the performance of supported Ni–Co bimetallic catalysts with different weight loadings of Co doping in DMO hydrogenation, the experiments were performed under fixed reaction conditions, as follows: P = 2.5 MPa, T = 180 °C, and LHSV = 0.50 h^{-1}. As shown in Table 2, the DMO hydrogenation on monometallic Ni and Co are comparable at a similar level, where the DMO conversion was obtained as 17% and 20% on 15Ni/SiO_2 and 15Co/SiO_2, respectively. Meanwhile, the selectivity for MG was 85% on both 15Ni/SiO_2 and 15Co/SiO_2. The major side products are ethylene glycol, ethanol, and methyl formate (MF). Considering the distinguished differences on the metal nanoparticle sizes of 15Ni/SiO_2 and 15Co/SiO_2, where the Ni nanoparticles (23.72 nm) are much larger than the Co nanoparticles (6.27 nm) according to the XRD measurement, it is clearly revealed that the intrinsic hydrogenation activity is higher on the active sites of Ni rather than that for Co.

Table 2 Reaction performances of various supported Ni–Co alloy catalysts

	Conversion (%)	Selectivity (%)					
Sample name	DMO	MG	EG	ET	MF	MA	Others
15Ni/SiO_2	17	85	3	7	1	0	4
15Ni–3Co/SiO_2	22	67	4	10	10	0	9
15Ni–10Co/SiO_2	51	92	4	3	0	0	1
15Ni–15Co/SiO_2	32	85	4	6	0	0	5
15Co/SiO_2	20	85	6	5	2	0	2

This conclusion is also supported by the H_2-TPD results, where the monometallic Ni owns both larger capability and stronger strength of hydrogen adsorption compared to monometallic Co. Therefore, the results suggest that the appropriate doping of other metals into Ni nanoparticles can be beneficial for the better dispersion of Ni atoms. At this point, according to the similar physicochemical properties, such as atomic diameters between Ni and Co, the bimetallic system of Ni and Co can at least enhance the effects of Ni redispersion. To identify this hypothesis, Co was doped within Ni nanoparticles. According to Table 2, when a small amount (3 wt%) of Co was added to 15 wt% of Ni, the DMO conversion was slightly promoted to 22% from 17% (absence of Co doping); however, the selectivity for MG dramatically decreased to 67% from 85% (absence of Co doping). Noteworthily, it needs to be emphasized that the selectivity for undesired products (ET and MF) reached the highest as 20% on 15Ni–3Co/SiO_2.

For the production of undesired ethanol from the deep hydrogenation of MG, two pathways may be proposed, where one is *via* "MG → EG → ET" and the other is "MG → MA → ET". The former route first proceeds with the hydrogenation of MG to EG and methanol, and then the hydrogenation-dehydration of EG to form ET and water. The latter route first proceeds with the hydrogenation-dehydration of MG to MA and water, and then the hydrogenation of MA to ET and methanol. Owing to the absence of MA product on all the prepared catalysts, the second route can be excluded. Therefore, in the first route, the ET production from deep hydrogenation of MG requires acid sites for the dehydration step from EG. Furthermore, the production of MF from MG is typically through the cracking of the C–C bond in the MG molecule, where this process usually demands acid sites or metal sites (*i.e.*, *via* hydrocracking). Therefore, the total selectivity control of ET and MF greatly relies on the capability of H_2 activation and acid sites on the catalyst surface. According to the H_2-TPD results, it was observed that 15Ni–3Co/SiO_2 and 15Ni–10Co/SiO_2 possess the highest capacity and strongest strength of hydrogen adsorption. According to the NH_3-TPD results, the total number of acid sites (including weak, medium and strong acid sites) decrease in the order of 15Ni–15Co/SiO_2 > 15Ni–3Co/SiO_2 > 15Ni–10Co/SiO_2, and the number of weak acid sites also follows the same order. In contrast, the number of medium and strong acid sites follows the sequence of 15Ni–3Co/SiO_2 > 15Ni–15Co/SiO_2 > 15Ni–10Co/SiO_2. Noteworthily, the number of total acid sites on 15Ni–3Co/SiO_2 and 15Ni–15Co/SiO_2 is close. In summary, the above-mentioned findings reveal that 15Ni–3Co/SiO_2 is the only sample that simultaneously possesses a large number of acid sites and metal sites. Especially, the highest strength of medium and strong acid sites exists on 15Ni–3Co/SiO_2. Considering the reaction pathways, these properties can lead to the highest total selectivity for ET and MF produced on 15Ni–3Co/SiO_2, in particular for the cracking of the C–C bond in MG to produce MF. However, this phenomenon of high total selectivity (ET and MF) was not reflected on other samples that possess either a large numbers of acid sites (*i.e.*, 15Co/SiO_2 and 15Ni–15Co/SiO_2) or metal sites (*i.e.*, 15Ni–15Co/SiO_2). In this regard, it can be concluded that the strength of the acid sites plays an important role in the product distribution, and especially it demonstrates the synergetic effect between the acid sites and metal sites during the DMO hydrogenation on 15Ni–3Co/SiO_2, leading to high selectivity for MF. Moreover, the high selectivity (9%) for other mixed products on the 15Ni–3Co/SiO_2 catalyst may also be due to its surface properties. Oppositely, only 1% of other mixed products was formed on 15Ni–10Co/SiO_2.

In the aspect of DMO conversion, when Co was doped into the Ni nanoparticles from 3 wt% to 10 wt%, the DMO conversion increased to 51% and the MG selectivity was promoted to 92%. In contrast, when the Co loading increased to 15 wt%, the DMO conversion diminished to 32% and the for MG decreased to 85%, which is the same as the monometallic Ni and Co catalysts. Based on the above-mentioned results, it is not difficult to find that there is one optimal point for the quantity of Co doping (10 wt%) to enhance both DMO conversion and MG selectivity. More specifically, in terms of DMO conversion, the reasons for the high DMO conversion on 15Ni–10Co/SiO_2 are attributed to the multiple physicochemical properties, such as the small particle size of the bimetallic catalysts, the outstanding capability of hydrogen activation, and the uniform and appropriate adsorption strength of DMO or key oxygenated intermediates, which can be supported by XRD, H_2-TPD and *in situ* CO-DRIFTS.

3.9.2 Effects of reaction temperature. To investigate the effects of reaction temperature on the 15Ni–10Co/SiO_2 catalyst, the DMO hydrogenation was carried out at various temperatures from 170 °C to 220 °C under the fixed pressure of 2.5 MPa and 0.50 h^{-1}. As displayed in Fig. 6(A), it is clear to see the positive impact of reaction temperature toward DMO conversion, where the conversion of DMO increased from 43% at 170 °C to 79% at 220 °C. Nonetheless, the selectivity for MG did not follow a similar trend as DMO conversion. As the reaction temperature increased, the selectivity for MG initially increased from 76% at 170 °C to

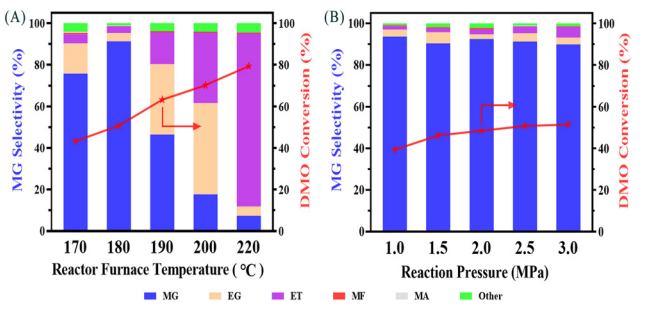

Fig. 6 (A) Result of the effect of reactor furnace temperature on the 15Ni–10Co/SiO_2 catalyst. (B) Result of the effect of reaction pressure on the 15Ni–10Co/SiO_2 catalyst.

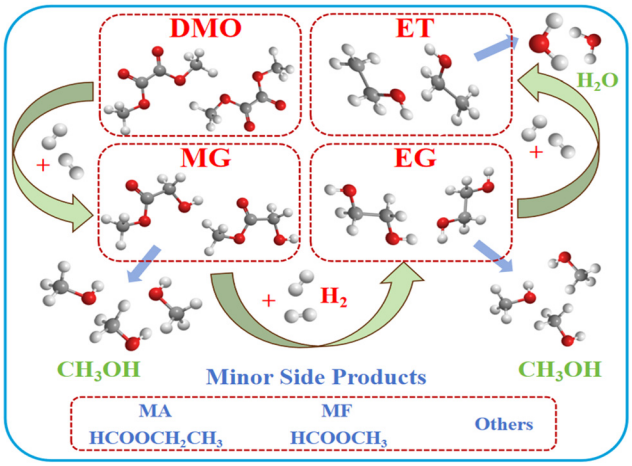

Scheme 1 Routes of DMO hydrogenation to various products.

91% at 180 °C, but then continuously decreased to 7% at 220 °C. Specifically, when the reaction temperature was 200 °C, ethylene glycol and ethanol become the two major hydrogenation products, where the selectivity was 44% and 34%, for ethylene glycol and ethanol, respectively. However, when the reaction temperature approached 220 °C, ethanol became the dominant product with the selectivity of 83%. The selectivity for MG and ethylene glycol were below 10% and 5%, respectively. According to the proposed reaction shown in Scheme 1, a series of sequential hydrogenation steps occur starting from DMO to MG to ethylene to ethanol; in addition, DMO can also be hydrogenated to methyl formate or methyl acetate (MA).[51,52] However, no formation of methyl acetate was detected in the tested temperature interval on 15Ni–10Co/SiO_2 in this work. Thus, the productivity of DMO sequential hydrogenation is very sensitive to the reaction temperature because of the effects on reaction favorability and stability of the key oxygenated intermediates. Therefore, according to the above-mentioned findings, it can reasonably be concluded that high reaction temperature is harmful for producing MG and the optimal hydrogenation temperature should be adjusted at around 180 °C on the 15Ni–10Co/SiO_2 catalyst.

3.9.3 Effects of reaction pressure. To investigate the effects of reaction pressure on the 15Ni–10Co/SiO_2 catalyst, DMO hydrogenation was carried out under various pressures from 1 MPa to 3 MPa at the fixed temperature of 180 °C and 0.50 h^{-1}. The experimental result is shown in Fig. 6(B). As the reactor pressure increased, the DMO conversion was not very sensitive, and gradually increased from 39% (1 MPa) to 51% (3 MPa). Essentially, the DMO conversion remained constant when the pressure was above 2.5 MPa. Considering the energy input and safety, it is sufficient to hold the reactor pressure as 2.5 MPa to obtain the maximum DMO conversion. Alternatively, no remarkable variation in the MG selectivity (~91%) was observed under the tested range of reactor pressure although a slight promotion of the selectivity for ethanol from 2% under 1 MPa to 6% under 3 MPa was observed. A very small amount of methyl formate was detected under all the pressures but no production of methyl acetate was noticed. This finding suggests that the reaction pressure does not significantly affect the favorability of sequential hydrogenation steps from DMO to ethylene glycol to ethanol on the 15Ni–10Co/SiO_2 catalyst. Thus, a reactor pressure of 2.5 MPa can be simultaneously beneficial for both DMO conversion and selectivity for MG.

3.9.4 Effects of space velocity. Based on the determination of Co doping loading, reaction temperature and reaction pressure, the one last factor to optimize the reaction efficiency of DMO hydrogenation to MG is the space velocity. To this end, a wide liquid hourly space velocity (LHSV) range was employed from 0.0625 h^{-1} to 1 h^{-1} to meticulously investigate the correlation between space velocity and DMO conversion or MG selectivity. As displayed in Fig. 7, at the fixed reaction condition where the temperature was 180 °C and reactor pressure was 2.5 MPa, the DMO conversion kept diminishing from 96% to 38% together with an increase in the space velocity from 0.0625 h^{-1} to 1 h^{-1}. This trend is sound to convey that the DMO conversion is very sensitive to the space velocity. Subsequently, DMO can be sufficiently activated and further converted on the catalyst surface with a longer contact time. Conversely, the selectivity for MG follows the promoting trend from 51% to 96%. Meanwhile, both the selectivity for ethylene glycol and ethanol decreased when the space velocity increased. In detail, the selectivity for ethylene glycol decreased from 32% to 2%, and the selectivity for ethanol decreased from 10% to 1%. Furthermore, it is worth noting that the absence of methyl acetate formation verifies that ethanol production is from ethylene glycol intermediate not the methyl acetate intermediate. According to the suggested reaction routes shown in Scheme 1, it is reasonable to conclude that the product distribution of DMO sequential hydrogenation with the sequence "MG → EG → ET" can be facilely mediated by varying the space velocity.

Due to the existence of opposite tendencies for DMO conversion and MG selectivity with respect to space velocity, it is necessary to quantify the yield of MG for its maximum

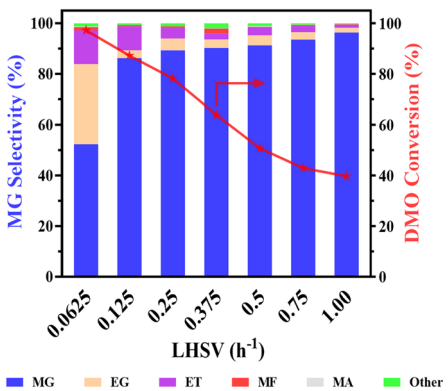

Fig. 7 Result of the effect of the space velocity on the 15Ni–10Co/SiO_2 catalyst.

production. In this respect, the yield of MG initially increased from 51% to 75% with the LHSV of 0.0625 h^{-1} and 0.125 h^{-1}, respectively. However, it kept decreasing to 38% when the LHSV was 1 h^{-1} because of the unceasing reduction of DMO conversion. Therefore, to achieve the highest yield of MG, the optimal point of liquid hourly space velocity should be at 0.125 h^{-1} on the 15Ni–10Co/SiO_2 catalyst at 180 °C and reactor pressure of 2.5 MPa. Under this condition, the optimized conversion of DMO and MG selectivity were 87% and 86%, respectively.

4. Conclusions

In summary, Ni and Co with higher hydrogenation efficiency and low cost were selected as active sites and Ni–Co bimetallic catalysts with different ratios were prepared *via* the equal-volume impregnation method. The well-dispersed Ni–Co alloy catalysts were constructed by doping Co elements into Ni, which had more excellent catalytic hydrogenation performance than the monometallic Ni or Co catalysts. The best catalytic performance was achieved on the 15Ni–10Co/SiO_2 catalyst with the conversion of DMO of 87% and MG selectivity of 86% at a mild temperature (180 °C). Combined with the characterization results, it was found that there is an effective bimetallic interaction between Ni and Co to form an alloy phase, further leading to changes in a series of properties, including the size of the metallic nanoparticle, capability of hydrogen adsorption, uniformity of active sites for CO adsorption and DMO (or key oxygenated intermediates) adsorption, and the surface acidity of the bimetallic catalysts. This work displayed the catalytic behaviors of DMO selective hydrogenation on non-precious Ni–Co alloy catalysts; simultaneously, it also provides meaningful guidance for the design of efficient Ni-based catalysts for the selective hydrogenation of oxygenates with multiple ester groups.

Data availability

The data supporting this article have been included in the ESI.†

Conflicts of interest

There are no conflicts to declare.

Acknowledgements

This work is supported by the National Key R&D Program of China (2023YFA1506302), the National Natural Science Foundation of China (U23A20112), and the Science and Technology Plan Fund of Yulin City (CXY-2022-141). C. R. C. acknowledges the Young Talent Support Plan of Shaanxi Province, the Shaanxi Technological Innovation Team (2024RS-CXTD-47), the CAS Youth Interdisciplinary Team, the Programme of Introducing Talents of Discipline to Universities (B23025), and the NSFC Center for Single-Atom Catalysis (22388102). X. G. acknowledges the financial support from Foundation of State Key Laboratory of Clean and Efficient Coal Utilization, Taiyuan University of Technology, China (MINYSKL202309), Natural Science Basic Research Program of Shaanxi Province at China (2024JC-YBQN-0071) and the Postdoctoral Research Project Fund of Shaanxi Province, China (No. 2023BSHEDZZ22).

References

1 J. W. Cottom, E. Cook and C. A. Velis, *Nature*, 2024, **633**, 101–108.
2 S. Krause, V. Ouellet, D. Allen, S. Allen, K. Moss, H. A. Nel, S. Manaseki-Holland and I. Lynch, *Cell Rep. Med.*, 2024, **5**, 101581.
3 M. H. Rahman and P. R. Bhoi, *J. Cleaner Prod.*, 2021, **294**, 126218.
4 K. Yamane, H. Sato, Y. Ichikawa, K. Sunagawa and Y. Shigaki, *Polym. J.*, 2014, **46**, 769–775.
5 K. Budak, O. Sogut and U. A. Sezer, *J. Polym. Res.*, 2020, **27**, 208.
6 C. K. S. Pillai and C. P. Sharma, *J. Biomater. Appl.*, 2010, **25**, 291–366.
7 P. Sharma, V. K. Gaur, R. Sirohi, S. Varjani, S. Hyoun Kim and J. W. C. Wong, *Bioresour. Technol.*, 2021, **325**, 124684.
8 P. Nair, G. R. Navale and M. S. Dharne, *Biomass Convers. Biorefin.*, 2021, **13**, 4555–4573.
9 F. M. Lamberti, L. A. Roman-Ramirez and J. Wood, *J. Polym. Environ.*, 2020, **28**, 2551–2571.
10 Z. Ai, *Professional Master's Degree*, East China University of Science and Technology, 2012.
11 D. Chen and Z. Zhao, *CN Pat.*, 1066650A, 1992.
12 B. Wang, K. Tian and G. Xu, *J. Nat. Gas Chem.*, 2005, **30**(4), 64–68.
13 L. Yan, *Professional Master's Degree*, East China University of Science and Technology, 2010.
14 L. Lin, P. Pan, Z. Zhou, Z. Li, J. Yang, M. Sun and Y. Yao, *Chin. J. Catal.*, 2011, **32**, 957–969.
15 R.-P. Ye, L. Lin, J.-X. Yang, M.-L. Sun, F. Li, B. Li and Y.-G. Yao, *J. Catal.*, 2017, **350**, 122–132.
16 H. Fan, J. Tan, Y. Zhu, H. Zheng and Y. Li, *J. Mol. Catal. A: Chem.*, 2016, **425**, 68–75.
17 H. Zheng, Y. Xue, Y. Niu, X. Gao, Y. Wang, G. Ding and Y. Zhu, *J. Chem. Technol. Biotechnol.*, 2022, **97**, 2572–2580.
18 D. Wang, C. Zhang, M. Zhu, F. Yu and B. Dai, *ChemistrySelect*, 2017, **2**, 4823–4829.
19 M. Abbas, Z. Chen, J. Zhang and J. Chen, *New J. Chem.*, 2018, **42**, 10290–10299.
20 H. Zhang, Y. Song, S. Wu, S. Yin, J. Zhao and J. Ren, *Appl. Catal., A*, 2024, **677**, 119710.
21 X. Wang, S. Qin, H. Zhang, J. Gong, W. Shu, C. Zhang, D. Wang and B. Dai, *ChemistrySelect*, 2023, **8**, e202300192.
22 G. Dong, Y. Cao, S. Zheng, J. Zhou, W. Li, F. Zaera and X. Zhou, *J. Catal.*, 2020, **391**, 155–162.
23 Z. Luo, Y. Shen, D. Fang, C. He, Y. Cao, W. Li, Y.-A. Zhu, J. Zhou and X. Zhou, *Mol. Catal.*, 2024, **559**, 114109.

24 J. Zhu, L. Cao, C. Li, G. Zhao, T. Zhu, W. Hu, W. Sun and Y. Lu, *ACS Appl. Mater. Interfaces*, 2019, **11**, 37635–37643.
25 Z. Zhuang, Y. Li, F. Chen, X. Chen, Z. Li, S. Wang, X. Wang, H. Zhu, Y. Tan and Y. Ding, *Chem. Commun.*, 2022, **58**, 1958–1961.
26 Z. Xia and S. Guo, *Chem. Soc. Rev.*, 2019, **48**, 3265–3278.
27 A. B. Lende, S. Bhattacharjee and C.-S. Tan, *ACS Sustainable Chem. Eng.*, 2021, **9**, 7224–7234.
28 B. Li, P. Gu, Y. Feng, G. Zhang, K. Huang, H. Xue and H. Pang, *Adv. Funct. Mater.*, 2017, **27**, 1605784.
29 A. J. Howarth, A. W. Peters, N. A. Vermeulen, T. C. Wang, J. T. Hupp and O. K. Farha, *Chem. Mater.*, 2016, **29**, 26–39.
30 Z. Ye, J.-M. Giraudon, N. Nuns, P. Simon, N. De Geyter, R. Morent and J.-F. Lamonier, *Appl. Catal., B*, 2018, **223**, 154–166.
31 K. S. W. Sing, *Pure Appl. Chem.*, 1985, **57**, 603–619.
32 Y. Chen, Z. Li, H. Jing and W. Li, *Meitan Xuebao*, 2023, **48**, 1413–1424.
33 J. Zhang, X. Liu, L. Deng, X. Liu, F. Li, R. Wang and C. Chen, *J. Alloys Compd.*, 2022, **925**, 166600.
34 L. Zhao, X. Mu, T. Liu and K. Fang, *Catal. Sci. Technol.*, 2018, **8**, 2066–2076.
35 X. Gao, Z. Tan, K. Hidajat and S. Kawi, *Catal. Today*, 2017, **281**, 250–258.
36 C. Chen, M. Zhou, P. Liu, B. K. Sharma and J. Jiang, *New J. Chem.*, 2020, **44**, 18906–18916.
37 S. W. Byun, H. Shin, W. Bin Bae, M. J. Hazlett, Y. Jin Kim, S. Jun Lee, M. Kim and S. B. Kang, *Chem. Eng. J.*, 2024, **481**, 148316.
38 K. Li, H. Liu, R. Zhang, L. Ling and B. Wang, *Appl. Surf. Sci.*, 2016, **390**, 7–16.
39 Y. Zhu, Y. Ma, Y. Sun, L. Wang, J. Ding, Y. Zhong, J. Zhang, L. Wang and Y. Li, *Renewable Energy*, 2023, **217**, 119222.
40 J. Luo, K. Kamasamudram, N. Currier and A. Yezerets, *Chem. Eng. Sci.*, 2018, **190**, 60–67.
41 F. Lónyi and J. Valyon, *Microporous Mesoporous Mater.*, 2001, **47**, 293–301.
42 X. Gai, D. Yang, R. Tang, M. Luo, P. Lu, C. Xing, R. Yang, Q. Ma and Y. Li, *Fuel*, 2022, **316**, 123337.
43 G. Zhao, H. Li, J. Si, Q. Nie, C. Meng, Y. Liu and Y. Lu, *ACS Sustainable Chem. Eng.*, 2021, **9**, 16719–16729.
44 H. Xu, Z.-X. Shi, Y.-X. Tong and G.-R. Li, *Adv. Mater.*, 2018, **30**, 1705442.
45 Z. Zhang, R. Liu, L. Huang and P. Liu, *J. Catal.*, 2024, **440**, 115824.
46 H. She, P. Yue, X. Ma, J. Huang, L. Wang and Q. Wang, *Appl. Catal., B*, 2020, **263**, 118280.
47 D. Xu, Z. Zhang, K. Tao and L. Han, *Dalton Trans.*, 2023, **52**, 2455–2462.
48 S. Vijay, W. Ju, S. Brückner, S.-C. Tsang, P. Strasser and K. Chan, *Nat. Catal.*, 2021, **4**, 1024–1031.
49 P. Arnoldy and J. A. Moulijn, *J. Catal.*, 1985, **93**, 38–54.
50 D. Song, J. Li and Q. Cai, *J. Phys. Chem. C*, 2007, **111**, 18970–18979.
51 R.-P. Ye, L. Lin, L.-C. Wang, D. Ding, Z. Zhou, P. Pan, Z. Xu, J. Liu, H. Adidharma, M. Radosz, M. Fan and Y.-G. Yao, *ACS Catal.*, 2020, **10**, 4465–4490.
52 Z. Luo, X. Xu, G. Dong, Y. Cao, S. Hu, G. Ye, Y.-A. Zhu, J. Zhou, W. Li and X. Zhou, *Chem. Eng. J.*, 2022, **450**, 138397.

